

# Preliminary Zircon Geochemistry of Northern Hogem Batholith, Quesnel Terrane, North-Central British Columbia (Parts of NTS 093M/16, 093N/13, 14, 094C/03–06, 094D/01, 08)

**G.O. Jones<sup>1</sup>**, Department of Earth and Atmospheric Sciences, University of Alberta, Edmonton, Alberta, gojones@ualberta.ca

**D.G. Pearson**, Department of Earth and Atmospheric Sciences, University of Alberta, Edmonton, Alberta

**A. Vezinet**, Department of Earth and Atmospheric Sciences, University of Alberta, Edmonton, Alberta

**Y. Luo**, Department of Earth and Atmospheric Sciences, University of Alberta, Edmonton, Alberta

**R.A. Stern**, Department of Earth and Atmospheric Sciences, University of Alberta, Edmonton, Alberta

**D. Milidragovic**, Natural Resources Canada, Geological Survey of Canada–Pacific, Vancouver, British Columbia

**L. Ootes**, British Columbia Geological Survey, British Columbia Ministry of Energy, Mines and Low Carbon Innovation, Victoria, British Columbia

Jones, G.O., Pearson, D.G., Vezinet, A., Luo, Y., Stern, R.A., Milidragovic, D. and Ootes, L. (2021): Preliminary zircon geochemistry of northern Hogem batholith, Quesnel terrane, north-central British Columbia (parts of NTS 093M/16, 093N/13, 14, 094C/03–06, 094D/01, 08); in *Geoscience BC Summary of Activities 2020: Minerals and Mining*, Geoscience BC, Report 2021-01, p. 105–120.

## Introduction

In 2018, the British Columbia Geological Survey initiated a three-year mapping program after Geoscience BC released the Search III airborne magnetic and radiometric data for the area between the Lorraine and Kemess porphyry deposits (Figures 1, 2; CGG Canada Services Ltd., 2018). The mapping program was initiated to update the bed-rock geology in the southern part of the Search III footprint, with a focus on northern Hogem batholith (Figures 1, 2; Ootes et al., 2019, 2020a, b).

This project was initiated as part of the bed-rock mapping program to study the details of magma genesis in the Hogem batholith and provide insights into the petrogenesis of plutonic suites that host porphyry style Cu-Au ( $\pm$ Mo) mineralization. The Thane Creek suite (ca. 196 Ma) hosts several Cu-Au porphyry occurrences (e.g., Cathedral prospect), while the Duckling Creek suite (ca. 180 Ma) hosts the Lorraine Cu-Au deposit, amongst other prospects and occurrences (Bath et al., 2014;

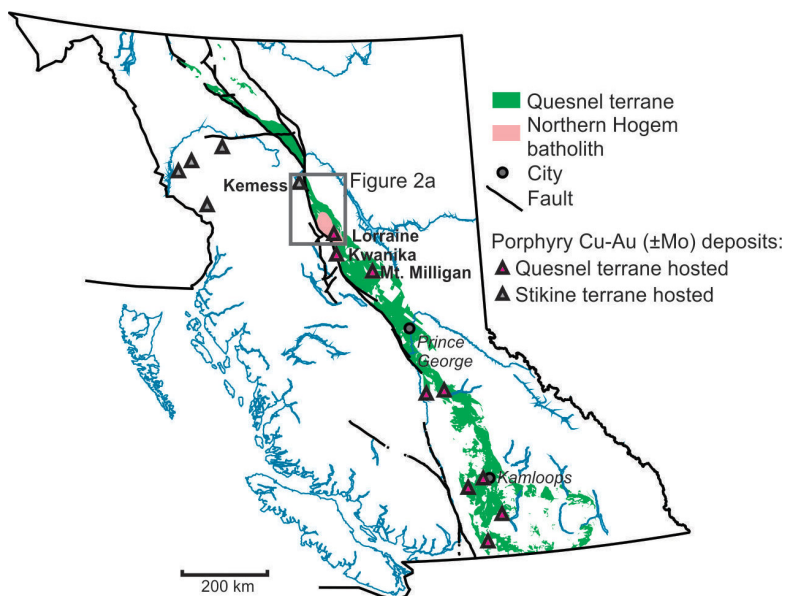


**Figure 1.** Geographic distribution of the Quesnel terrane (with the Hogem batholith highlighted) and major Triassic–Jurassic porphyry deposits in British Columbia. Porphyry deposits of interest in this study are labelled. The footprint of Figure 2a, which includes the Search III geophysical data, is outlined in grey. The study area is in northern Hogem batholith, which was covered by the southeastern extent of the Search III survey. Geology from BC Geological Survey (2020).

Devine et al., 2014). This paper introduces a multi-isotopic study from these two intrusive suites. Interpretation of crystallization ages has been previously presented (Bath et al., 2014; Devine et al., 2014; Ootes et al., 2020b) and the focus of this contribution is an integrated multi-isotopic and trace-element study of zircon, and the application of

<sup>1</sup>The lead author is a 2020 Geoscience BC Scholarship recipient.

This publication is also available, free of charge, as colour digital files in Adobe Acrobat® PDF format from the Geoscience BC website: <http://geosciencebc.com/updates/summary-of-activities/>.

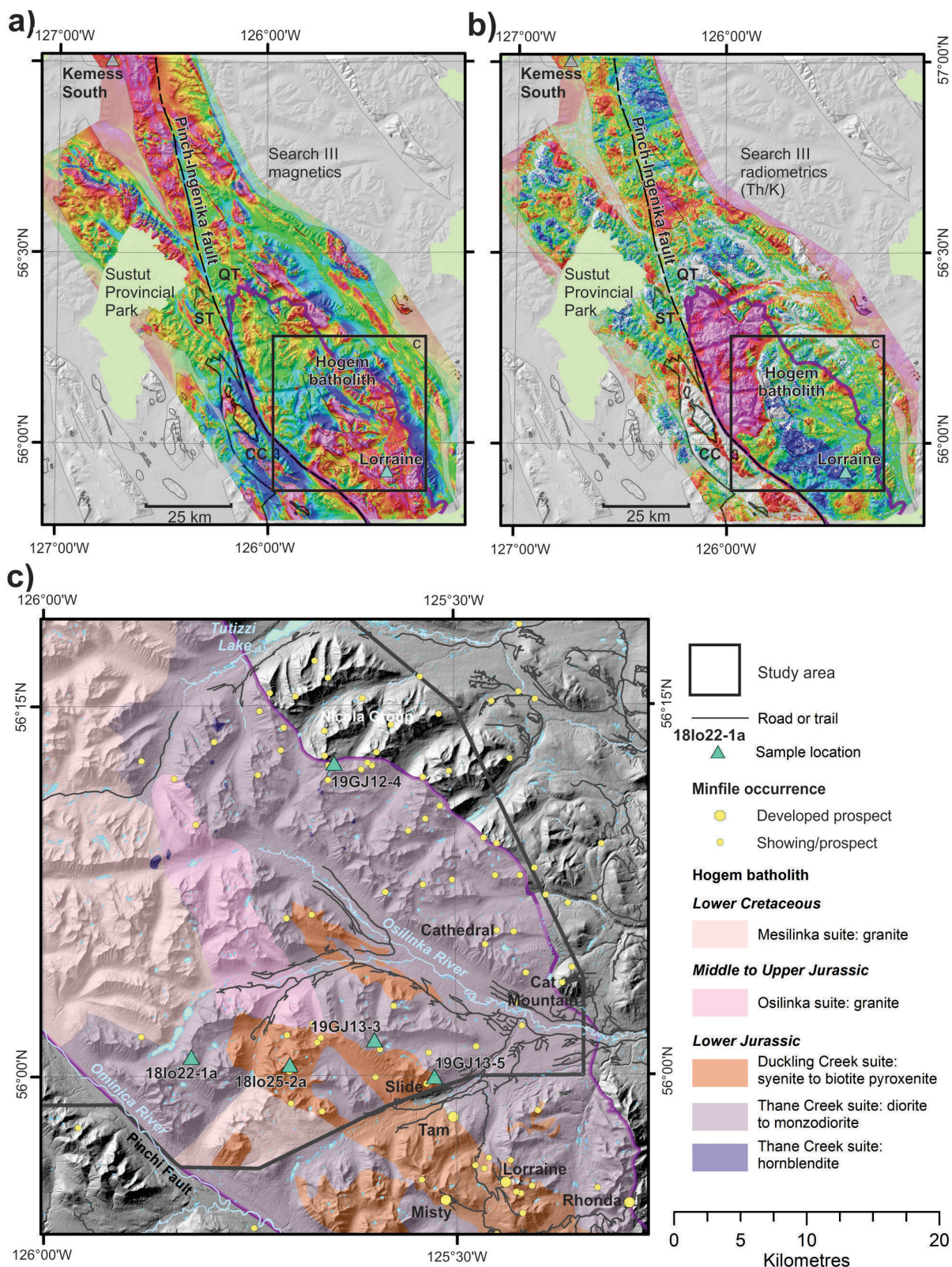


**Figure 2.** Results from the Search III airborne survey: **a)** radio magnetic indicator (RMI) and **b)** radiometric (Th/K; CGG Canada Services Ltd., 2018). Warm colours correspond to higher magnetism and Th/K values, and cool colours correspond to lower magnetism and Th/K values. The Pinchi-Ingenika fault separates the Quesnel terrane (QT) on the east from the Stikine (ST) and Cache Creek (CC) terranes on the west. The northern part of the Hogem batholith is outlined in purple. The Lorraine and Kemess South porphyry deposits are shown for reference. **c)** Bedrock geology of northern Hogem batholith. The black line depicts the location of the study area and limit of mapping by Ootes et al. (2019, 2020a, b). The geology to the south of the black line is from Devine et al. (2014). Prospects and developed prospects that are labelled are discussed in the text.

these data for understanding magmatic-metal enrichment and carrying capacity in the Hogem batholith.

Porphyry deposits typically have alteration haloes that are produced by chemical and mineralogical alteration of the hostrocks (e.g., Byrne et al., 2016). This paper focuses on magmatic phases that are spatially, genetically and temporally associated with porphyry-style mineralization, and sampling was conducted away from mineralized or heavily altered zones. Such an approach provides a background perspective on igneous petrogenesis and regional, versus deposit scale, insights into the controls on mineralization potential of the magma (i.e., fertility; e.g., Richards, 2013). The data collected for this study are from single zircon crystals and include U-Pb, Lu-Hf and oxygen isotopes, and trace elements. Isotopic U-Pb analysis allows for the determination of crystallization ages; Lu-Hf analysis provides insight into the nature of the parental magma and its source reservoir(s); oxygen isotopes establish if the magmatic source has been recycled following exposure to the hydrosphere; and the trace-element data allow estimates of temperature and oxidation state during crystallization.

## Regional Geology

The northern part of the Hogem batholith was mapped by Armstrong (1946), Lord (1948, 1949), Armstrong and Roots (1948, 1954), Roots (1954), Woodsworth (1976) and Ootes et al. (2019, 2020a, b). The southern part of the Hogem batholith was subdivided by Garnett (1972, 1978). Mapping by Ferri et al. (2001a, b) and Schiarizza and Tan (2005) focused on the Takla Group (referred to herein as the Nicola Group; cf. Ootes et al., 2020b) but left the northern part of the Hogem batholith largely undivided. Nixon and Peatfield (2003), Bath et al. (2014) and Devine et al. (2014) studied the Lorraine porphyry Cu-Au deposit, hosted in the Duckling Creek suite southeast of the study area, and provided isotopic ages and whole-rock geochemistry for mineralization and the hostrocks.

## Thane Creek Suite

The eastern and southwestern parts of the study area (Figure 2c) are underlain by diorite to quartz monzodiorite and lesser hornblendite of the Thane Creek suite, the oldest intrusive rocks in northern Hogem batholith (Ootes et al., 2019, 2020a, b). Diorite crosscuts and commingles with the hornblendite. Where commingling is present, the rocks are texturally and compositionally heterogeneous in terms of amphibole, plagioclase and magnetite abundances.

### Hornblendite

Black to ‘salt and pepper’, medium-grained to pegmatitic hornblendite forms  $\leq 100$  m wide plutons scattered through diorite of the Thane Creek suite (Figure 2c); see Ootes et al. (2019) for outcrop photos. Dark green amphibole crystals, with rare corroded clinopyroxene cores, predominate and

range from medium to coarse grained. Plagioclase, where present, is interstitial between amphibole and ranges from fine to coarse grained. Biotite, generally medium grained, is a common accessory mineral in the hornblendites, in concentrations ranging from 0 to 20%. Accessory euhedral titanite and euhedral to subhedral crystals of apatite are also common. Magnetite abundance in hornblendite varies (mostly  $\leq 5\%$ ), and these rocks have a strong magnetic signature (Figure 2a). Epidote is a secondary alteration mineral in the hornblendite and generally forms  $\leq 5\%$  of the rock. Trace amounts of disseminated pyrite and chalcopyrite occur and, in a few small outcrops ( $\sim 1$  m<sup>2</sup>), chalcopyrite constitutes a few percent of the rock. Some of the sulphide-bearing rocks have local malachite or iron-rust staining on weathered surfaces. The hornblendites are entirely within diorite and display both sharp and diffuse contacts, the latter indicating magma commingling. The hornblendites are interpreted as comagmatic with the diorite plutons and represent either crystal cumulates formed from a more primitive parental magma or injections of a hydrous mafic to ultramafic magma into a predominantly dioritic chamber. A sample of plagioclase-bearing pegmatitic hornblendite yielded a chemical-abrasion isotope dilution–thermal ionization mass spectrometry (CA-ID-TIMS) zircon U-Pb crystallization age of  $197.55 \pm 0.11$  Ma (Ootes et al., 2020b).

### Diorite to Quartz Monzodiorite

The eastern and southwestern parts of northern Hogem batholith are underlain mostly by green- and white-weathering to black- and white-weathering, equigranular, medium- to coarse-grained diorite that is foliated to locally mylonitic (Figure 2c). Along the eastern and northern margins of northern Hogem batholith, diorite of the Thane Creek suite intruded Nicola Group volcano-sedimentary rocks (Ferri et al., 2001a, b; Schiarizza and Tan, 2005; Ootes et al., 2020a). The diorite consists mostly of plagioclase and hornblende but locally transitions to units with more significant amounts of quartz and K-feldspar (quartz diorite, quartz monzodiorite, monzodiorite, granodiorite) and gabbro. Accessory phases include clinopyroxene (as corroded cores to amphibole), euhedral to subhedral titanite, magnetite and apatite. Epidote is locally common and interpreted as an alteration product. The diorite locally contains biotite, in some cases in much greater abundance than amphibole. The relatively potassic phases contain blotchy pink K-feldspar in the groundmass, which is accompanied by mint-green weathering in outcrop; these zones correspond to biotite- and epidote-rich phases, where plagioclase has been altered to clay minerals, amphibole is rare and titanite locally displays highly corroded grain boundaries. These features may indicate either late magmatic or secondary potassic alteration. The diorite contains variable abundances of magnetite; this variation could be from magmatic fractionation, secondary alteration or both.

The magnetic variation is evident on the airborne magnetic map (Figure 2a) and from magnetic susceptibility measurements (Ootes et al., 2019).

The diorite crosscuts and commingles with the hornblende (Ootes et al., 2019). Where there is commingling, the rocks are texturally and compositionally heterogeneous in terms of amphibole, plagioclase and magnetite concentrations. In some locations, the combined effects of mixing with enclaves, magmatic differentiation and K-alteration resulted in textural and compositional variations that are too small to show at the scale of the map (Ootes et al., 2019, 2020a). The diorite locally contains xenoliths of layered, fine-grained green rock, possibly derived from the Nicola Group. The diorite is locally stained with malachite and rarely contains disseminated chalcopyrite (<1%).

In the southeastern part of northern Hogem batholith, a diorite sample yielded a CA-ID-TIMS zircon U-Pb crystallization age of  $196.61 \pm 0.19$  Ma. This sample was taken ~30 m away from the location of a ca. 197.5 Ma hornblende sample referred to above (Ootes et al., 2020b). The result is comparable to, albeit younger than, a  $204.0 \pm 0.4$  Ma diorite at the Cat Mountain prospect in the eastern Thane Creek suite (Figure 2c; Mortensen et al., 1995) and a  $200.9 \pm 0.2$  Ma gabbro-diorite body at the Rhonda Cu prospect, 20 km south of the study area (Figure 2c; Devine et al., 2014). The Thane Creek diorite sample that yielded the ca. 196.6 Ma age also yielded an  $^{40}\text{Ar}/^{39}\text{Ar}$  biotite step-heating age of ca. 124 Ma, interpreted to record postdeformation cooling (Ootes et al., 2020b).

### Duckling Creek Suite

The south-southeastern part of the study area is underlain by quartz-undersaturated rocks of the Duckling Creek suite (Figure 2c; Ootes et al., 2019); this was called the ‘Duckling Creek syenite complex’ by Woodsworth (1976), Garnett (1978), Nixon and Peatfield (2003) and Devine et al. (2014). The Duckling Creek suite is mostly syenite to monzonite, with lesser monzodiorite and local zones of biotite pyroxenite. South of the study area, Devine et al. (2014) identified three stages of the Duckling Creek suite and constrained the timing with the following U-Pb zircon ages: 1) biotite pyroxenite (ca. 182–178.5 Ma); 2) predominantly K-feldspar–porphyritic syenite to monzonite (ca. 178.8–178.4 Ma); and 3) massive syenite and pegmatite (ca. 177–175 Ma). All three phases exist in the study area. The biotite pyroxenite is black weathering and locally contains megascopic phenocrysts (up to 0.5 cm) of white-weathering apatite. It is generally preserved at higher elevations and traceable over areas of tens to hundreds of metres, where it is extensively crosscut by syenite to monzonite and lesser monzodiorite. These more intermediate to felsic rocks range from equigranular to porphyritic to pegmatitic. Porphyritic varieties contain tabular, com-

monly zoned, K-feldspar phenocrysts (up to 5 cm long) that are set in a groundmass of equigranular green pyroxene and lesser albite, amphibole, magnetite, titanite and apatite. Rhythmic magmatic layering, defined by varying felsic and mafic mineral ratios and alignment of K-feldspar phenocrysts, is common. The entire unit has moderate to strong magnetism (Figure 2a), with areas of highest magnetism spatially associated with biotite pyroxenite. Biotite pyroxenite zones are locally stained with malachite and contain disseminated chalcopyrite.

Amphibole separated from a K-feldspar porphyritic syenite sample yielded an  $^{40}\text{Ar}/^{39}\text{Ar}$  step-heating age of ca. 177.6 Ma (Ootes et al., 2020b). This result overlaps, within uncertainty, with a previously reported  $^{40}\text{Ar}/^{39}\text{Ar}$  biotite age of  $177.1 \pm 0.9$  Ma for a similar syenite sample to the south (Devine et al., 2014). These ages are best interpreted as cooling of the pluton through the closure temperature of hornblende (~550°C).

### Mineralization

The Hogem batholith and the surrounding Nicola Group host porphyry-style deposits and prospects, including one producer (Mount Milligan; Figure 1). The most significant developed prospect in northern Hogem batholith is the Lorraine Cu-Au deposit, containing 6.42 million tonnes of indicated resource at 0.62% Cu and 0.23 g/t Au, and 28.82 million tonnes of inferred resource at 0.45% Cu and 0.19 g/t Au (Figures 1, 2c; Giroux and Lindinger, 2012). The Lorraine deposit is hosted by the biotite-pyroxenite phase of the Duckling Creek suite (Bath et al., 2014; Devine et al., 2014), which also hosts other developed prospects (Tam, Misty) and prospects/showings (e.g., Slide; Figure 2c).

The Thane Creek suite hosts a number of porphyry Cu-Au prospects and showings (e.g., Cathedral; Figure 2c). The Rhonda developed prospect (Figure 2c) is hosted by Rhonda-Dorothy gabbro (ca. 200 Ma; Devine et al., 2014), which is correlative with the Thane Creek suite. The Cat Mountain prospect is hosted in Nicola Group volcanic rocks that are intruded by dikes of the Thane Creek suite (ca. 204 Ma; Mortensen et al., 1995). A number of other Cu-Au prospects occur throughout the Thane Creek, Duckling Creek and Nicola Group rocks (Figure 2c; Ootes et al., 2019).

### Field and Laboratory Work

Zircon U-Pb, Lu-Hf, oxygen-isotope and trace-element geochemistry has become commonly used in igneous-petrogenetic studies (e.g., Lee et al., 2020; Sagan et al., 2020). Zircon geochemistry is a powerful tool, providing insight into the nature and antiquity of the magma source and evolution. This paper presents preliminary data for the

oldest locally mineralized intrusive phases of the Hogen batholith (i.e., the Thane Creek and Duckling Creek suites).

During fieldwork and sampling in 2018 and 2019, five samples were acquired from across the batholith to represent the geochemical heterogeneity of the intrusive suites (Figure 2c). Most samples were collected from areas lacking obvious alteration related to porphyry mineralization. The exception is sample 19GJ13-5a, which was collected next to the Slide prospect (Figure 2c) from outcrop exposures that also contain Cu mineralization. A single grab sample with chalcopyrite, collected 7 m north of 19GJ13-5a, yielded 0.07 wt. % Cu (19GJ13-5b; Ootes et al., 2020b).

Sample preparation was completed at the University of Alberta. Approximately 1 kg of sample was cut into centimetre-size pieces using a diamond-blade rock saw. These pieces were disaggregated using the SELFRAG laboratory electronic-pulse disaggregation system in the Canadian Centre for Isotopic Microanalysis (CCIM) to yield high-quality mineral separates. The mineral separates were sieved and panned to separate fine-grained (<355 µm), high-density minerals. The high-density mineral separates were examined using a stereo microscope to hand-pick clear, euhedral zircon grains. These zircons were set in epoxy mounts and polished to expose the grain midsections. Back-scattered electron (BSE), cathodoluminescence (CL) and secondary electron (SE) images of the zircon crystals were obtained on a scanning electron microscope at CCIM. These images were used to select spots for microanalysis.

For this study, a detailed workflow was designed prior to the analytical work because single zircon grains were to be used for multiple analyses. Acquisition of zircon oxygen-isotope data by secondary-ion mass spectrometry (SIMS) analysis, using a Cameca IMS 1280 multicollector ion microprobe, was completed first according to standard CCIM operating procedures (e.g., Vezinet et al., 2018) because this is the least destructive analytical method and requires precision-polished grain mounts. The SIMS analysis is sensitive to grain-mount topography, as the beam configuration involves focusing a primary  $^{133}\text{Cs}^+$  ion beam at an angle onto the sample to produce negative secondary ions ( $^{18}\text{O}^-$  and  $^{16}\text{O}^-$ ). After oxygen-isotope data collection by SIMS, zircons were investigated by laser-ablation inductively coupled plasma–mass spectrometry (LA-ICP-MS). Zircon U-Pb data were collected first, followed by trace elements and Lu-Hf. The LA-ICP-MS method involves focusing a RESOLUTION™ 193 nm ArF excimer laser, equipped with a 2-volume Laurus-Technic S-155 ablation cell, on a solid sample to ablate fine particles that are then transported via argon gas to a Thermo Fisher Scientific Element-XR™ (U-Pb and trace elements) or Thermo Fisher Scientific Neptune Plus™ (Lu-Hf) mass spectrometer for analysis. A preliminary subset of the U-Pb and Lu-Hf analyses was carried out simultaneously on a portion of the

same ablated material using the laser-ablation split-stream (LASS) ICP-MS technique (e.g., Fisher et al., 2014) and reduced with the software described in Fisher et al. (2017). The LA-ICP-MS analytical method was used for this study because it is relatively fast and cost effective, can produce large datasets and provides the opportunity to analyze specific within-grain growth zones. However, this method sacrifices precision, compared to more precise solution methods, such as thermal ionization-mass spectrometry (TIMS).

## Results

Magmatic-crystallization ages and Lu-Hf and oxygen-isotope results ( $\delta^{18}\text{O}$ ) obtained from zircon analyses are summarized in Table 1. All uncertainties are reported at the  $2\sigma$  (95%) confidence level. Both single-zircon  $^{206}\text{Pb}/^{238}\text{U}$  dates and interpreted magmatic-crystallization ages are plotted on Figures 3 and 4. The magmatic-crystallization ages are from this study, Ootes et al. (2020b) and Devine et al. (2014)

### Radiogenic Lu-Hf Isotopes

The results of Lu-Hf analyses are presented as the  $^{176}\text{Hf}/^{177}\text{Hf}$  ratio of a sample at the time of crystallization (t) relative to the  $^{176}\text{Hf}/^{177}\text{Hf}$  ratio of the chondritic uniform reservoir (CHUR), which is expressed as  $\epsilon\text{Hf}_t$  (uncertainty calculated using the Excel template of Ickert, 2013):

$$\epsilon\text{Hf}_t = \left( \frac{(^{176}\text{Hf}/^{177}\text{Hf})_{\text{SAMPLE}(t)}}{(^{176}\text{Hf}/^{177}\text{Hf})_{\text{CHUR}(t)}} - 1 \right) \times 10000,$$

$$\text{where } ^{176}\text{Hf}/^{177}\text{Hf}_t = ^{176}\text{Hf}/^{177}\text{Hf}_{(\text{measured})} - ^{176}\text{Lu}/^{177}\text{Hf} \times e^{[(\lambda^{176}\text{Lu} \times t) - 1]},$$

$$^{176}\text{Hf}/^{177}\text{Hf}_{\text{CHUR}(\text{measured})} = 0.282785 \pm 1, \quad ^{176}\text{Lu}/^{177}\text{Hf}_{\text{CHUR}} = 0.0336 \pm 1 \text{ (Bouvier et al., 2008),}$$

$$\text{and } \lambda^{176}\text{Lu} = 1.867 \times 10^{-11} \text{ (Söderlund et al., 2004).}$$

When using  $\epsilon\text{Hf}_t$  to determine the relative contributions of crust and mantle in the magma source, it is useful to have a comparable end-member rock suite. The estimated Hf isotopic ratio at time of rock formation is commonly compared to the CHUR and the depleted-mantle–evolution curve. Depleted mantle is calculated using the  $^{176}\text{Hf}/^{177}\text{Hf}$  ratio through time based on  $^{176}\text{Lu}/^{177}\text{Hf}$  and  $^{176}\text{Hf}/^{177}\text{Hf}_{\text{measured}}$  values of mid-ocean–ridge basalts (Chauvel and Blichert-Toft, 2001; Figures 3a, b). However, the depleted mantle may not be the best estimate of the composition of the mantle source to the Hogen batholith. The Stuhini Group in Stikine terrane has picritic tuffs that represent mantle-derived melts minimally contaminated by crustal interaction (Milidragovic et al., 2018). The Hogen batholith is part of Quesnel terrane and the Stuhini Group is part of Stikine terrane, but these two terranes have a remarkably similar geological history (e.g., Dostal et al., 1999), making the

**Table 1.** Summary of secondary-ion mass spectrometry (SIMS) and laser-ablation inductively coupled plasma-mass spectrometry (LA-ICP-MS) results for Thane Creek suite and Duckling Creek suite samples. Uncertainties are reported at the 2 $\sigma$  level. Abbreviation: MSWD, mean square of weighted deviates.

Sample name	18J13-5a		18J13-3		18J13-2a		18J13-1a		19J12-4	
	Duckling Creek	Duckling Creek	Thane Creek	Thane Creek	Duckling Creek	Thane Creek	Thane Creek	Thane Creek	Thane Creek	Thane Creek
Suite										
Lithology	Syenite	Syenite	Monzodiorite	Monzodiorite	Syenite	Hornblende	Hornblende	Diorite	Diorite	Diorite
Interpreted crystallization age	ca. 175 Ma	ca. 179 Ma	ca. 197 Ma	ca. 197 Ma	ca. 179 Ma	ca. 198 Ma	ca. 198 Ma	ca. 207 Ma	ca. 207 Ma	ca. 207 Ma
$^{176}\text{Hf}/^{177}\text{Hf}$ range	0.282899±52–0.282979±38	0.282907±30–0.282970±32	0.282928±29–0.282988±31	0.282928±29–0.282988±31	0.282907±30–0.282970±32	0.282901±43–0.282984±42	0.282901±43–0.282984±42	0.282898±74–0.282972±54	0.282898±74–0.282972±54	0.282898±74–0.282972±54
$^{176}\text{Hf}/^{177}\text{Hf}$ median	0.282934	0.282933	0.282949	0.282949	0.282933	0.282948	0.282948	0.282948	0.282948	0.282948
$^{176}\text{Hf}/^{177}\text{Hf}$ weighted mean	0.282940±7	0.282936±4	0.282954±5	0.282954±5	0.282940±7	0.282944±6	0.282944±6	0.282947±11	0.282947±11	0.282947±11
No. of analyses	29/29	39/39	40/40	40/40	39/39	42/42	42/42	11	11	11
MSWD	0.86	1.15	0.93	0.93	1.15	1.24	1.24	0.48	0.48	0.48
$^{176}\text{Lu}/^{177}\text{Hf}$ range	0.000560±36–0.002340±390	0.000220±5–0.005789±25	0.000600±120–0.002020±100	0.000600±120–0.002020±100	0.000560±36–0.002340±390	0.000105±1–0.002033±42	0.000105±1–0.002033±42	0.000301±13–0.003630±520	0.000301±13–0.003630±520	0.000301±13–0.003630±520
$^{176}\text{Lu}/^{177}\text{Hf}$ median	0.00109	0.001426	0.001227	0.001227	0.00109	0.000759	0.000759	0.001760	0.001760	0.001760
$\Sigma\text{Hf}$ range	7.9±1.9 - 10.5±1.4	8.2±1.8 - 10.1±1.0	9.3±1.1 - 11.5±1.2	9.3±1.1 - 11.5±1.2	7.9±1.9 - 10.5±1.4	8.2±1.6 - 11.1±1.5	8.2±1.6 - 11.1±1.5	8.4±2.7 - 11.0±2.0	8.4±2.7 - 11.0±2.0	8.4±2.7 - 11.0±2.0
$\Sigma\text{Hf}$ Median	9.02	9.11	9.99	9.99	9.02	9.86	9.86	10.1	10.1	10.1
$\Sigma\text{Hf}$ weighted mean	9.2±0.3	9.1±0.2	10.1±0.2	10.1±0.2	9.2±0.3	9.8±0.2	9.8±0.2	10.1±0.5	10.1±0.5	10.1±0.5
No. of analyses	29/29	38/38	40/40	40/40	29/29	42/42	42/42	11	11	11
MSWD	0.8	1.08	0.85	0.85	0.8	0.98	0.98	0.5	0.5	0.5
$\delta^{18}\text{O}_{\text{VSMOW}}$ (%) range	5.48±0.19–6.50±0.18	6.20±0.22–6.72±0.18	5.22±0.21–6.05±0.18	5.22±0.21–6.05±0.18	5.48±0.19–6.50±0.18	5.77±0.25–6.30±0.24	5.77±0.25–6.30±0.24	4.95±0.19–6.03±0.20	4.95±0.19–6.03±0.20	4.95±0.19–6.03±0.20
$\delta^{18}\text{O}_{\text{VSMOW}}$ (%) median	6.17	6.57	5.58	5.58	6.17	6.02	6.02	5.54	5.54	5.54
$\delta^{18}\text{O}_{\text{VSMOW}}$ (%) weighted mean	6.15±0.03	6.57±0.03	5.57±0.03	5.57±0.03	6.15±0.03	6.01±0.03	6.01±0.03	5.53±0.04	5.53±0.04	5.53±0.04
No. of analyses	38/39	39/40	53/55	53/55	38/39	43/43	43/43	22/22	22/22	22/22
MSWD	3.05	1.1	0.65	0.65	3.05	1.16	1.16	11	11	11

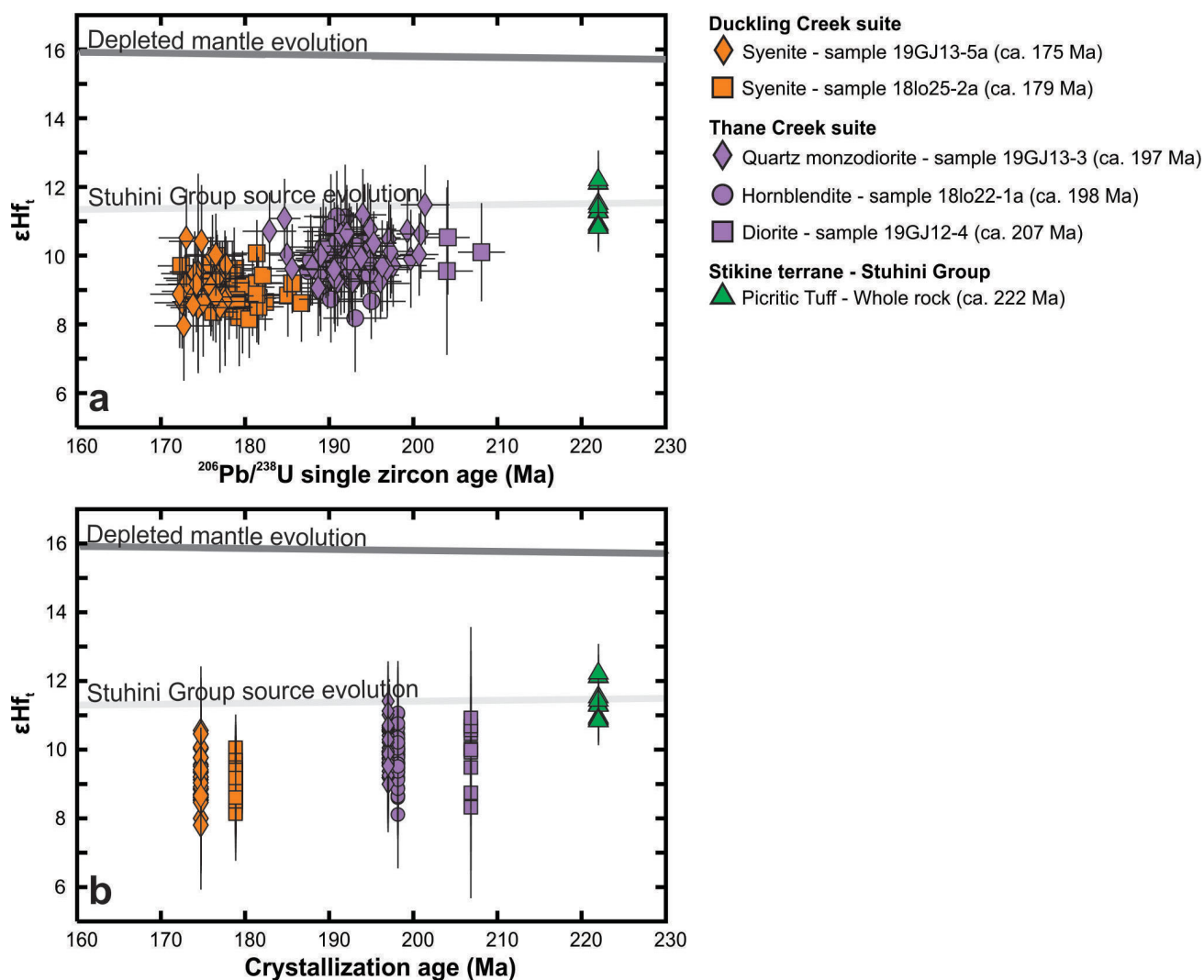


**Figure 3.** Plot of single-zircon  $\epsilon Hf_t$  (calculated at time (t) of crystallization) for multiple Duckling Creek and Thane Creek suite samples across the Hagem batholith plotted versus **a)** laser-ablation inductively coupled plasma–mass spectrometry (LA-ICP-MS)  $^{206}Pb/^{238}U$  single-zircon date (Ma) and **b)** crystallization U-Pb ages determined by thermal ionization-mass spectrometry (TIMS) for the Thane Creek diorite (ca. 197 Ma) and the Duckling Creek syenite (ca. 178 Ma), which have been previously reported (Devine et al., 2014; Ootes et al., 2020b). Interpreted crystallization ages on Figure 3b include data from G.O. Jones (unpublished data, 2020), Ootes et al. (2020b) and Devine et al. (2014). The depleted mantle (DM) Hf-evolution curve was calculated assuming present  $^{176}Hf/^{177}Hf_{DM} = 0.28325$  and  $^{176}Lu/^{177}Hf_{DM} = 0.0384$  (Chauvel and Blichert-Toft, 2001). The Stuhini picrite Hf-evolution curve was constructed assuming average present  $^{176}Hf/^{177}Hf = 0.283086$  and  $^{176}Lu/^{177}Hf = 0.0279$ , calculated from results in Milidragovic et al. (2018).

Stuhini picrite the best estimate of Quesnel terrane mantle. Milidragovic et al. (2018) posited that Late Triassic asthenospheric mantle underlying Stikine terrane, and by extrapolation the Quesnel terrane mantle, was less radiogenic than the depleted mantle at 222 Ma (Figures 3a, b). As such, in Figure 3a and b, the Hagem batholith  $\epsilon Hf_t$  values are also compared to Stuhini picrite, with a Hf evolution curve calculated using the average  $^{176}Lu/^{177}Hf$  and  $^{176}Hf/^{177}Hf_{measured}$  values from whole-rock analyses of Milidragovic et al. (2018).

The  $\epsilon Hf_t$  values of zircon from the Thane Creek suite generally overlap, but are less radiogenic than, the calculated time-evolved  $\epsilon Hf_t$  of the Stuhini Group picrite (Figure 3).

The oldest sample (19GJ12-4), a ca. 207 Ma diorite, has the most juvenile  $\epsilon Hf_t$  signature, with a weighted mean of  $10.1 \pm 0.5$ . The ca. 198 Ma hornblendite (18lo22-1a) is more evolved than the diorite, with a weighted mean  $\epsilon Hf_t$  of  $9.8 \pm 0.2$ . The ca. 197 Ma monzodiorite (19GJ13-3) has a weighted mean  $\epsilon Hf_t$  of  $10.1 \pm 0.2$ , indistinguishable from the older diorite sample.

The oldest Duckling Creek syenite sample (18lo25-2a; ca. 179 Ma) is the most evolved (Figure 3) and has a weighted mean  $\epsilon Hf_t$  of  $9.1 \pm 0.2$ . The ca. 175 Ma Duckling Creek syenite (19GJ13-5a) is slightly more juvenile, with a weighted mean of  $9.2 \pm 0.3$ . The ca. 175 Ma syenite  $\epsilon Hf_t$

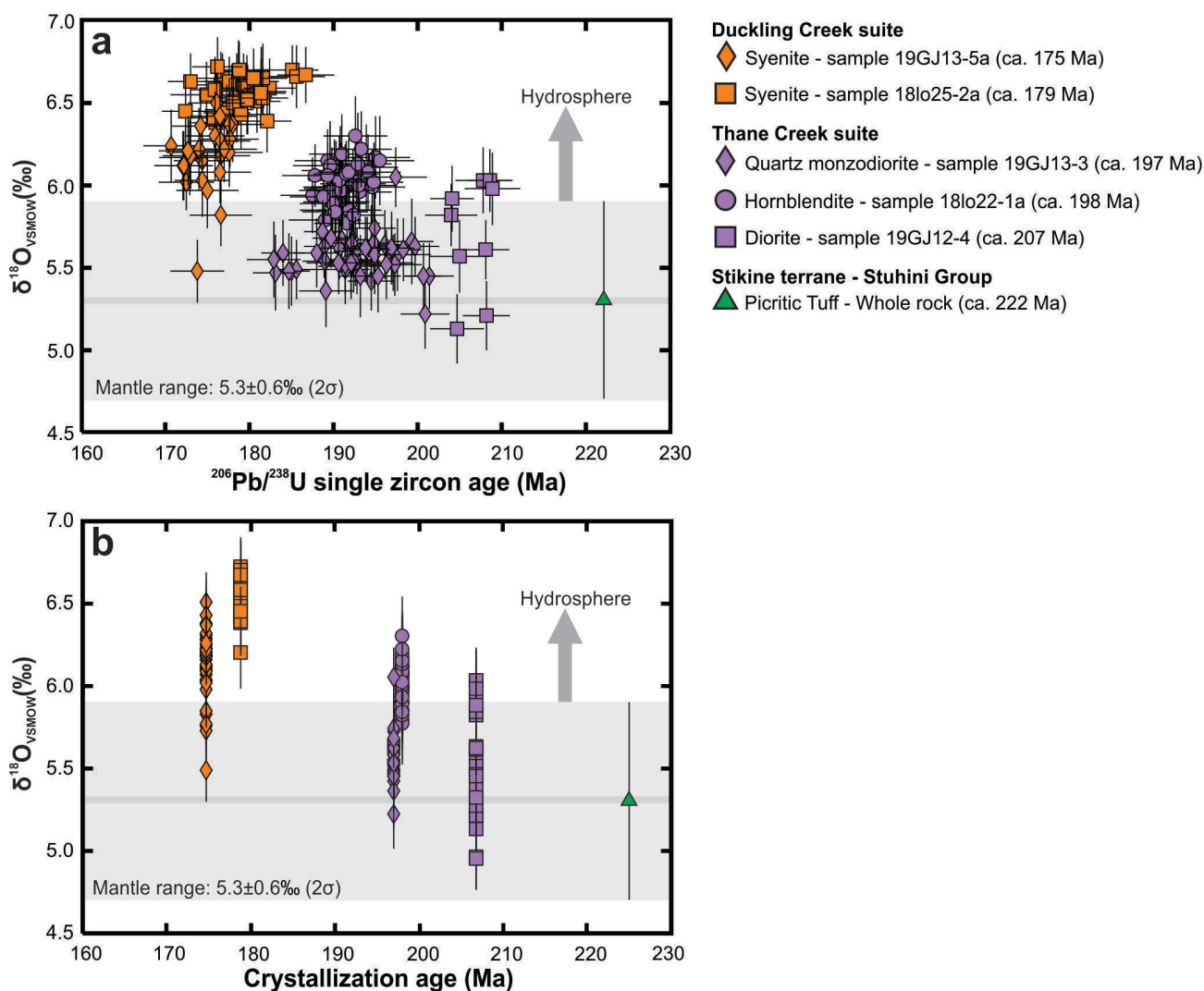


**Figure 4.** Plot of single-zircon  $\delta^{18}\text{O}$  for multiple Duckling Creek and Thane Creek suite samples across the Hogen batholith versus **a)** laser-ablation inductively coupled plasma–mass spectrometry (LA-ICP-MS)  $^{206}\text{Pb}/^{238}\text{U}$  single-zircon date (Ma) and **b)** crystallization ages (explained in Figure 3b caption). Mantle zircon  $\delta^{18}\text{O}$  from Valley et al. (2005).

overlaps, within uncertainty, the Stuhini picrite, whereas the ca. 179 Ma syenite is slightly more evolved (Figure 3).

### Oxygen Isotopes

The results of oxygen-isotope analyses are presented as the  $^{18}\text{O}/^{16}\text{O}$  ratio relative to average seawater (VSMOW), which is expressed as  $\delta^{18}\text{O}$  in per mille (‰):

$$\delta^{18}\text{O} = \left( \frac{(^{18}\text{O}/^{16}\text{O})_{\text{SAMPLE}}}{(^{18}\text{O}/^{16}\text{O})_{\text{VSMOW}}} - 1 \right) \times 1000,$$

where  $^{18}\text{O}/^{16}\text{O}_{\text{VSMOW}} = 0.0020052$  (Baertschi, 1976).

On Figure 4, the Hogen batholith  $\delta^{18}\text{O}$  data are compared to the average mantle zircon  $\delta^{18}\text{O}$  value of  $5.3 \pm 0.6\text{‰}$  ( $2\sigma$ ; Valley et al., 2005), which is invariant through time. The ambient mantle  $\delta^{18}\text{O}$  value is assigned to the Stuhini picrite

(Figure 4a, b), as oxygen isotope data are not available for those Stuhini samples (Milidragovic et al., 2018).

The  $\delta^{18}\text{O}$  data for the Thane Creek suite are mostly within the mantle range. The ca. 207 Ma diorite has the largest range in  $\delta^{18}\text{O}$  and a weighted mean of  $5.53 \pm 0.04\text{‰}$ . The ca. 198 Ma hornblendite has a higher  $\delta^{18}\text{O}$  signature that is slightly above the mantle range, with a weighted mean of  $6.01 \pm 0.03\text{‰}$ . The ca. 197 Ma monzodiorite is indistinguishable from the older diorite sample, with a weighted mean  $\delta^{18}\text{O}$  of  $5.57 \pm 0.03\text{‰}$ .

Zircon from the ca. 179 Ma Duckling Creek syenite has the highest  $\delta^{18}\text{O}$  signature, higher than mantle values, with a weighted mean of  $6.57 \pm 0.03\text{‰}$ . The ca. 175 Ma Duckling Creek syenite has a larger range in  $\delta^{18}\text{O}$  values and a weighted mean of  $6.15 \pm 0.03\text{‰}$ . This weighted mean is

above the mantle values, with only a few individual analyses overlapping it (Figure 4).

### Europium and Titanium Concentrations

Europium concentration data are presented as chondrite-normalized Eu anomalies ( $\text{Eu}_N/\text{Eu}_N^*$ ), calculated as follows:

$$\frac{\text{Eu}_N}{\text{Eu}_N^*} = \frac{\text{Eu}_N}{\sqrt{(\text{Sm}_N \times \text{Gd}_N)}}$$

where N signifies C1 chondrite normalized. C1 chondrite values are from Sun and McDonough (1989).

The ca. 207 Ma Thane Creek diorite, ca. 197 Ma Thane Creek monzodiorite and ca. 175 Ma Duckling Creek syenite have strong negative Eu anomalies ( $\text{Eu}_N/\text{Eu}_N^* \sim 0.3\text{--}0.5$ ; Figure 5). The ca. 198 Ma Thane Creek hornblende has a moderate to weak negative Eu anomaly ( $\text{Eu}_N/\text{Eu}_N^* \sim 0.6\text{--}0.8$ ) and the ca. 179 Ma Duckling Creek syenite has a weak negative to positive Eu anomaly ( $\text{Eu}_N/\text{Eu}_N^* \sim 0.8\text{--}1.2$ ; Figure 5).

Titanium concentration data are presented as Ti-in-zircon temperatures, calculated using the zircon crystallization thermometer of Watson et al. (2006), assuming rutile saturation:

$$T(^{\circ}\text{C})_{\text{Zircon}} = \frac{5080 \pm 30}{(6.01 \pm 0.03) \cdot \log(\text{Ti})} - 273,$$

where Ti signifies the measured concentration of Ti in zircon (ppm).

The ca. 207 Ma diorite has the highest concentration and largest range of Ti ( $\sim 10\text{--}22$  ppm), resulting in Ti-in-zircon temperatures of  $\sim 740\text{--}817^{\circ}\text{C}$  (Figure 6). The ca. 198 Ma hornblende has lower Ti concentrations and a range of  $\sim 2\text{--}7$  ppm, with Ti-in-zircon temperatures of  $\sim 639\text{--}711^{\circ}\text{C}$ . The ca. 197 Ma monzodiorite overlaps the hornblende Ti range, with concentrations of  $\sim 4\text{--}9$  ppm and Ti-in-zircon temperatures of  $\sim 677\text{--}729^{\circ}\text{C}$  (Figure 6).

The ca. 179 Ma Duckling Creek syenite sample has the lowest Ti concentrations, ranging from below the limit of detection to 4 ppm, and Ti-in-zircon temperatures of  $\sim 484\text{--}669^{\circ}\text{C}$ . The ca. 175 Ma Duckling Creek syenite has a higher concentration and larger range in Ti ( $\sim 6\text{--}15$  ppm) and Ti-in-zircon temperatures ( $\sim 699\text{--}778^{\circ}\text{C}$ ; Figure 6).

### Discussion

Zircon oxygen-isotope data are useful for igneous petrogenetic studies because oxygen isotopes are not significantly fractionated in the mantle (Valley et al., 2005). Zircon  $\delta^{18}\text{O}$  values higher than the mantle range indicate that  $^{18}\text{O}$  is preferentially fractionated relative to  $^{16}\text{O}$ , which re-

quires the magmatic source to have experienced low-temperature, near-surface processes (Valley et al., 2005). This would typically occur during interaction with the hydrosphere and implies that the parental magma melted or interacted with crust that was recycled. Enrichment of  $\delta^{18}\text{O}$  relative to the average mantle range in some Hogem zircons may reflect the incorporation of crustal material in the magma or magma source (Figures 4, 7). This crustal material may be derived externally (i.e., recycled supracrustal material or assimilation of host rock) or internally (i.e., remelting of the Hogem batholith that has interacted with the hydrosphere).

The samples from the Thane Creek suite have  $\delta^{18}\text{O}$  signatures within the range of the average mantle and  $\epsilon\text{Hf}_t$  values that are slightly less radiogenic than the Hf-evolution curve of the Stuhini Group picrite (Figure 3). This implies that the Thane Creek suite crystallized from predominantly juvenile magmas of mantle- or near-mantle composition (Figure 7).

The ca. 179 Ma syenite has  $\delta^{18}\text{O}$  values higher than the mantle range and  $\epsilon\text{Hf}_t$  values that are less radiogenic than the Stuhini picrite and Thane Creek suite (Figures 3, 4, 7), possibly indicating minor crustal contamination of the magma. The ca. 175 Ma Duckling Creek syenite has mantle-like  $\epsilon\text{Hf}_t$  values but elevated  $\delta^{18}\text{O}$  (Figures 3, 4, 7), implying the magma was juvenile and with a near-mantle composition, albeit with fractionated oxygen. The ca. 175 Ma syenite sample was obtained close to the previously mentioned Slide showing/prospect (19GJ13-5a; Figure 2c). The results from this sample may have implications for characterizing magmatic-mineralization potential in the Hogem area.

Preliminary  $\delta^{18}\text{O}$  and  $\epsilon\text{Hf}_t$  results from Hogem S-type granites (Early Cretaceous; G.O. Jones, unpublished data, 2020) are compared to those from the Thane Creek and Duckling Creek suites on Figure 7. The S-type granites have fractionated  $\delta^{18}\text{O}$  characteristic of magmas with a source that was recycled through the hydrosphere. The most evolved Duckling Creek and Thane Creek samples have lower  $\delta^{18}\text{O}$  and higher  $\epsilon\text{Hf}_t$  signatures than the Hogem S-type granite field, indicating these intrusions have more primitive source characteristics.

Samples from both the Thane Creek and Duckling Creek suites do not show a simple temporal trend in Hf-O systematics. The Thane Creek hornblende and the oldest Duckling Creek syenite have the most evolved Hf-O compositions. The variability in  $\delta^{18}\text{O}$  and  $\epsilon\text{Hf}_t$ , unrelated to time, indicate variability in the magma sources and/or variability in crustal contamination during magma genesis and evolution.

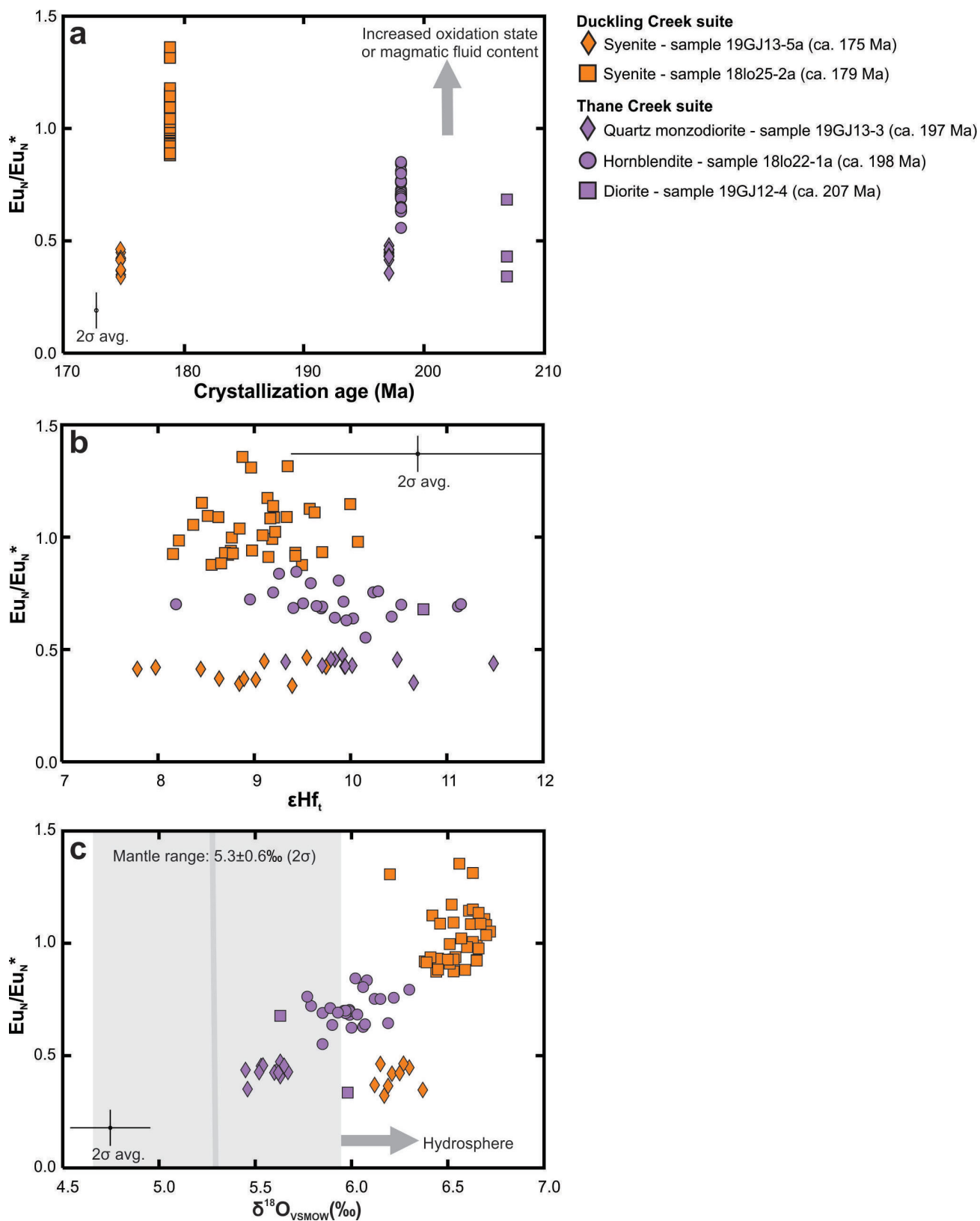


**Figure 5.** Plot of single-zircon Eu anomaly ( $Eu_N/Eu_N^*$ ) for multiple samples of the Duckling Creek and Thane Creek suites across the Hagem batholith versus **a**) crystallization ages (explained in Figure 3b caption), **b**)  $\epsilon Hf_t$ , and **c**)  $\delta^{18}O$ . The darker grey line in Figure 5c represents the  $\delta^{18}O$  of average mantle zircon (5.3‰) and the light-grey shading represents the 2σ uncertainty of this value (0.6‰; Valley et al., 2005).

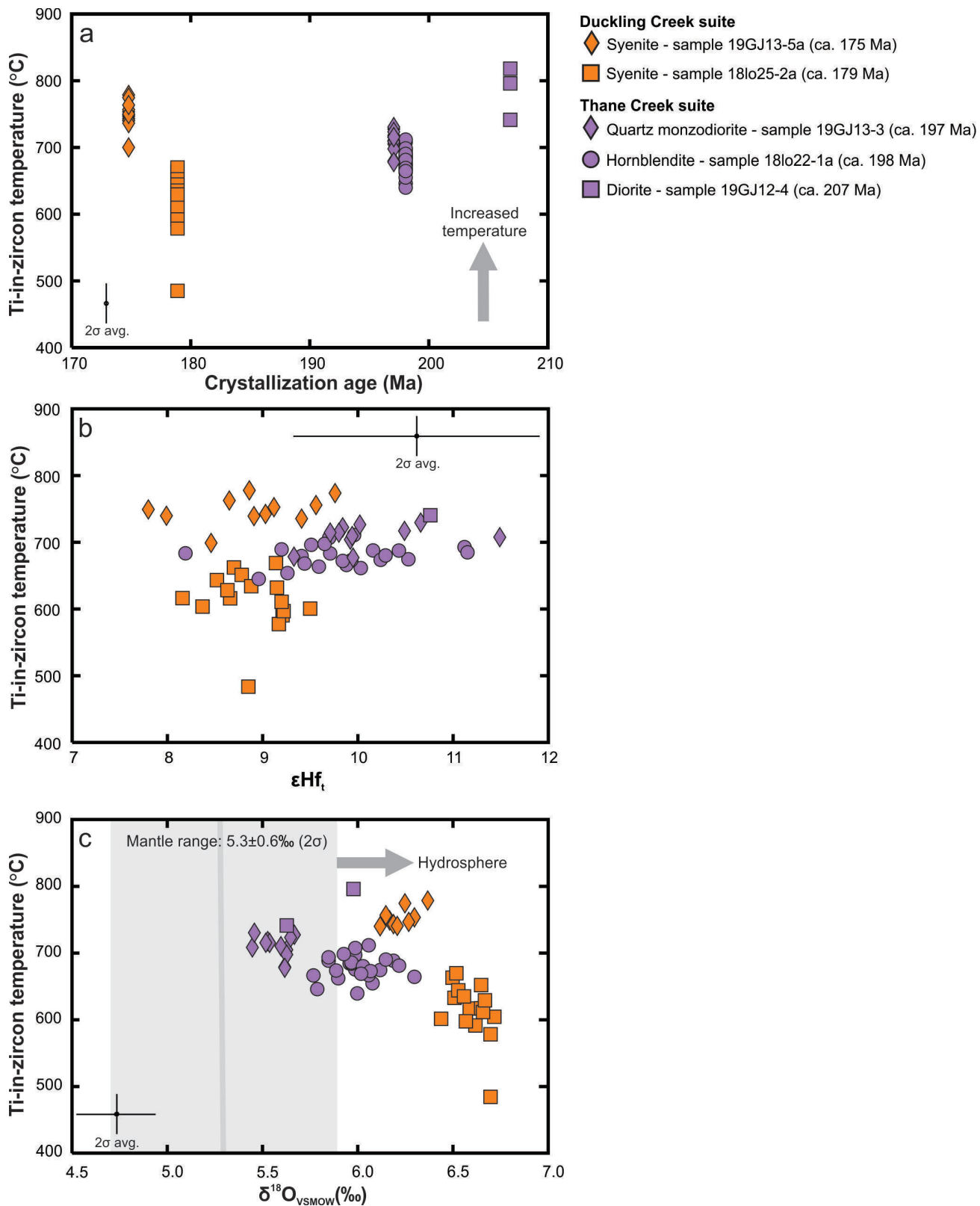


**Figure 6.** Plot of single Ti-in-zircon temperature for multiple samples of the Duckling Creek and Thane Creek suites across the Hogen batholith versus **a**) crystallization ages (explained in the caption for Figure 3b), **b**)  $\epsilon Hf_t$ , and **c**)  $\delta^{18}O$ .

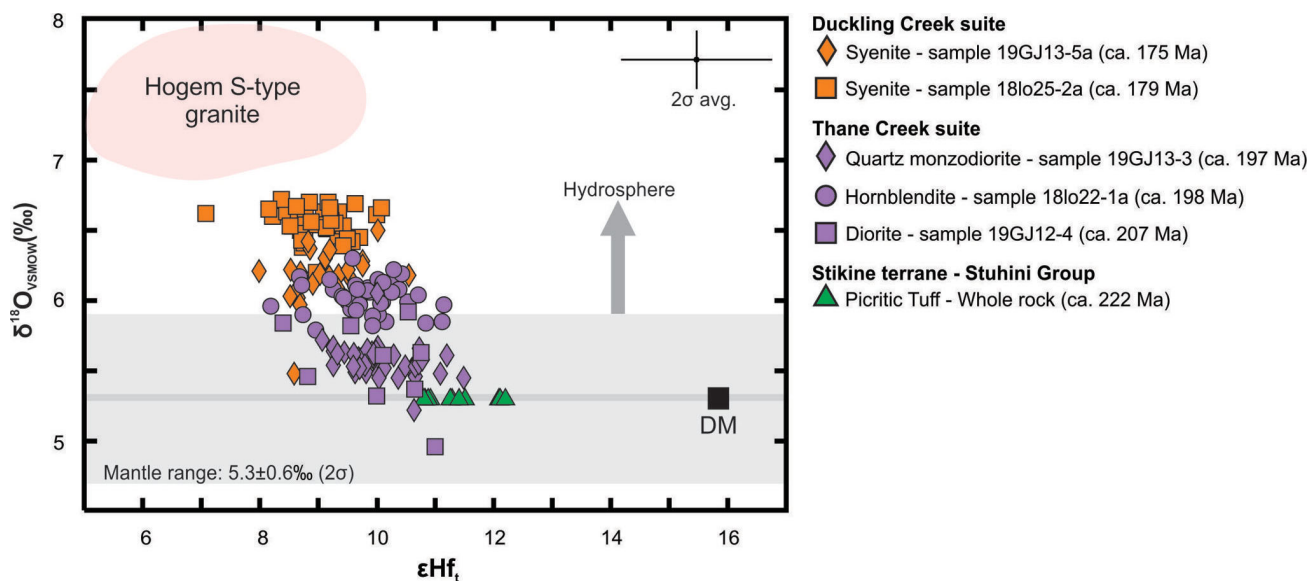


**Figure 7.** Plot of single-zircon  $\epsilon Hf_t$  versus  $\delta^{18}O$ . Depleted mantle (DM) Hf data are from Chauvel and Blichert-Toft (2001). Mantle zircon  $\delta^{18}O$  is from Valley et al. (2005). Hogem S-type granite field is from G.O. Jones (unpublished data, 2020).

Europium anomalies in zircon are potential proxies for oxygen fugacity during crystallization in a magma (Shen et al., 2015; Lee et al., 2017; Lee et al., 2020) and/or magmatic-water content (Lu et al., 2016). Elevated magmatic-water content suppresses plagioclase crystallization, which results in increased Eu in the magma and crystallizing zircon (Wilke and Behrens, 1999; Ballard et al., 2002; Lee et al., 2017). In oxidized magmas,  $Eu^{2+}$  can be converted to  $Eu^{3+}$ , which cannot be substituted into the plagioclase crystal lattice but can be incorporated into zircon (Ballard et al., 2002; Lee et al., 2017). This results in a less negative Eu anomaly in zircon, reflecting relative magmatic-water content and oxidation state (Lee et al., 2017).

Titanium-in-zircon concentrations are used to calculate crystallization temperatures, assuming rutile saturation in the magma (Watson et al., 2006). The assumption of rutile saturation in the magma implies zircon  $TiO_2$  and  $SiO_2$  activities of 1. The Ti-in-zircon temperatures presented here are minimum temperatures, as the  $TiO_2$  activities of these zircons are likely less than 1. A lower zircon  $TiO_2$  activity will result in an increased crystallization-temperature estimate, up to  $\sim 70^\circ C$  higher (Ferry and Watson, 2007). Additionally, these Ti-in-zircon temperatures represent only single temperature points in the overall temperature range of the cooling and crystallizing magmas but are useful for comparisons between intrusive suites. The ca. 207 Ma diorite,

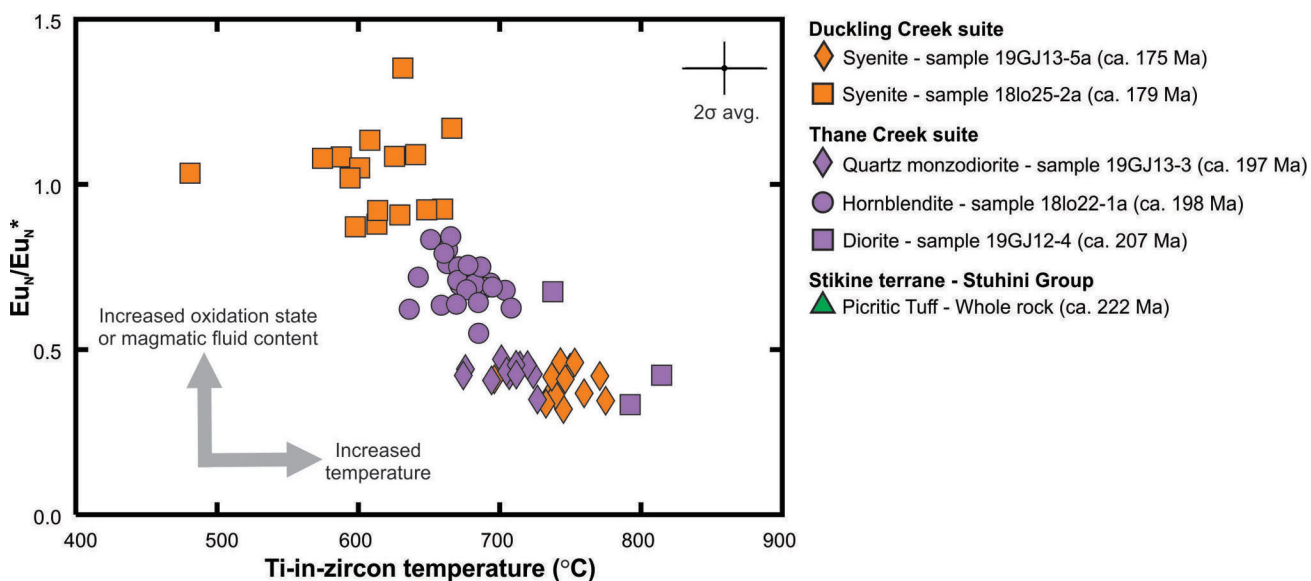


**Figure 8.** Plot of single titanium-in-zircon temperature versus Eu anomaly ( $Eu_N/Eu_N^*$ ).

ca. 197 Ma monzodiorite and ca. 175 Ma syenite have higher Ti-in-zircon temperatures (~677–817°C) and stronger negative Eu anomalies (~0.3–0.5) compared to the ca. 198 Ma hornblendite and ca. 179 Ma syenite (~484–711°C; ~0.6–1.2; Figure 8). Higher Ti concentrations and stronger Eu anomalies imply the zircons crystallized from higher temperature and less oxidized or less hydrous magmas.

The Eu anomaly and Ti data have differing relationships with  $\delta^{18}\text{O}$  and  $\varepsilon\text{Hf}_i$ . The  $\text{Eu}_N/\text{Eu}_N^*$  and Ti-in-zircon temperature versus  $\delta^{18}\text{O}$  show discrete clusters, indicating that Eu anomaly and Ti vary with  $\delta^{18}\text{O}$  (Figures 5c, 6c). However, Figures 5b and 6b show significant overlap in individual zircon  $\varepsilon\text{Hf}_i$  values, despite slight variances in the weighted mean  $\varepsilon\text{Hf}_i$  between samples. This overlap implies the source of oxygen-isotope fractionation in the magmas may also influence the Eu anomaly and Ti concentration.

## Conclusions and Future Work

The porphyry-hosting Thane Creek and Duckling Creek suites have  $\delta^{18}\text{O}$ ,  $\varepsilon\text{Hf}_i$ , Ti and  $\text{Eu}_N/\text{Eu}_N^*$  signatures that are variable through time. These variations indicate changes in the crustal input (crustal recycling in the source or crustal contamination of a magma), temperature, and oxidation state or fluid content of magma sources that formed these intrusive suites. These differences likely had an impact on magma fertility (i.e., the metal-carrying and concentration-capacity of the magmas), as water-rich and oxidized magmas are necessary to increase the metal contents of hydrothermal fluids that contribute to porphyry mineralization (e.g., Sillitoe, 2010).

The zircon geochemistry (U-Pb, Lu-Hf,  $\delta^{18}\text{O}$  and trace elements) used in this study will help further characterize the magmas that formed the Hogem batholith, determine differences between intrusive suites and phases within those suites, and assess the impact of these characteristics on magma fertility. Future analytical work includes additional SIMS  $\delta^{18}\text{O}$  and LA-ICP-MS Lu-Hf and trace-element analyses. Estimating zircon crystallization temperatures using the Ti-in-zircon thermometer with more accurate zircon  $\text{TiO}_2$  and  $\text{SiO}_2$  activities, comparing Ce and Eu anomalies, and evaluating the zircon and whole-rock geochemical dataset in relation to porphyry-style mineralization will further characterize the magmatic evolution of northern Hogem batholith.

## Acknowledgments

This study is funded by the BC Geological Survey and the Diamond Exploration Research Training School (DERTS). The latter is funded by the Natural Sciences and Engineering Research Council of Canada (NSERC) Collaborative Research and Training Experience (CREATE) Program and the University of Alberta. The principal author grate-

fully acknowledges support from Geoscience BC and NSERC scholarships. The authors thank L. Aspler and D. Thorkelson for constructive reviews of this manuscript.

Natural Resources Canada, Lands and Minerals Sector contribution 20200542

## References

- Armstrong, J.E. (1946): Aiken Lake (south half), British Columbia; Geological Survey of Canada, Paper 46-11, 1 map at 1 inch to 2 mile scale, URL <<https://open.library.ubc.ca/cIRcle/collections/ubctheses/831/items/1.0107001>> [September 2020].
- Armstrong, J.E. and Roots, E.F. (1948): Geology and mineral deposits of the Aiken Lake map-area, British Columbia; Geological Survey of Canada, Paper 48-5, 46 p., URL <<https://doi.org/10.4095/101388>>.
- Armstrong, J.E. and Roots, E.F. (1954): Aiken Lake, Cassiar District, British Columbia; Geological Survey of Canada, Map 1030A, scale 1 inch to 4 miles, URL <<https://doi.org/10.4095/106855>>.
- Baertschi, P. (1976): Absolute  $^{18}\text{O}$  content of standard mean ocean water; Earth and Planetary Science Letters, v. 31, no. 3, p. 341–344, URL <[https://doi.org/10.1016/0012-821X\(76\)90115-1](https://doi.org/10.1016/0012-821X(76)90115-1)>.
- Ballard, J.R., Palin, J.M. and Campbell, I.H. (2002): Relative oxidation states of magmas inferred from Ce(IV)/Ce(III) in zircon: application to porphyry copper deposits of northern Chile; Contributions to Mineralogy and Petrology, v. 144, p. 347–364, URL <<https://doi.org/10.1007/s00410-002-0402-5>>.
- Bath, A.B., Cooke, D.R., Friedman, R.M., Faure, K., Kamenetsky, V.S., Tosdal, R.M. and Berry, R.F. (2014): Mineralization, U-Pb geochronology, stable isotope geochemistry of the Lower Main Zone of the Lorraine deposit, north-central British Columbia: a replacement-style alkalic Cu-Au porphyry; Economic Geology, v. 109, p. 979–1004, URL <<https://doi.org/10.2113/econgeo.109.4.979>>.
- BC Geological Survey (2020): MapPlace GIS internet mapping system; BC Ministry of Energy, Mines and Low Carbon Innovation, BC Geological Survey, URL <<http://www.MapPlace.ca>> [October 2020].
- Bouvier, A., Vervoort, J.D. and Patchett, P.J. (2008): The Lu-Hf and Sm-Nd isotopic composition of CHUR: constraints from unequilibrated chondrites and implications for the bulk composition of terrestrial planets; Earth and Planetary Science Letters, v. 273, no. 1–2, p. 48–57, URL <<https://doi.org/10.1016/j.epsl.2008.06.010>>.
- Byrne, K., Lesage, G., Gleeson S.A. and Lee, R.G. (2016): Large-scale sodic-calcic alteration around porphyry Cu systems: examples from the Highland Valley Copper district, Guichon batholith, south-central British Columbia; in Geoscience BC Summary of Activities 2016, Report 2017-1, p. 213–222, URL <[http://cdn.geosciencebc.com/pdf/SummaryofActivities2016/SoA2016\\_Byrne.pdf](http://cdn.geosciencebc.com/pdf/SummaryofActivities2016/SoA2016_Byrne.pdf)> [September 2020].
- CGG Canada Services Ltd. (2018): Geophysical survey report: MIDAS high resolution magnetic and radiometric survey, Search Project, Phase III; Geoscience BC, Report 2018-02, 72 p., URL <[http://cdn.geosciencebc.com/project\\_data/GBCReport2018-02/GBCR2018-02-Report.pdf](http://cdn.geosciencebc.com/project_data/GBCReport2018-02/GBCR2018-02-Report.pdf)> [September 2020].

- Chauvel, C. and Blichert-Toft, J. (2001): A hafnium isotope and trace element perspective on melting of the depleted mantle; *Earth and Planetary Science Letters*, v. 190, p. 137–151, URL <[https://doi.org/10.1016/S0012-821X\(01\)00379-X](https://doi.org/10.1016/S0012-821X(01)00379-X)>.
- Devine, F., Chamberlain, C.M., Davies, A.G.S., Friedman, R. and Baxter, P. (2014): Geology and district-scale setting of tilted alkalic porphyry Cu-Au mineralization at the Lorraine deposit, British Columbia; *Economic Geology*, v. 109, no. 4, p. 939–977, URL <<https://doi.org/10.2113/econgeo.109.4.939>>.
- Dostal, J., Gale, V. and Church, B.N. (1999): Upper Triassic Takla Group volcanic rocks, Stikine terrane, north-central British Columbia: geochemistry, petrogenesis, and tectonic implications; *Canadian Journal of Earth Sciences*, v. 36, p. 1483–1494, URL <<https://doi.org/10.1139/e99-048>>.
- Ferri, F., Dudka, S.F., Rees, C. and Meldrum, D. (2001a): Geology of the Aiken Lake area, north-central British Columbia, NTS 94C/5, 6 and 12; BC Ministry of Energy, Mines and Low Carbon Innovation, BC Geological Survey, Geoscience Map 2001-10, scale 1:50 000, URL <[http://cmscontent.nrs.gov.bc.ca/geoscience/PublicationCatalogue/GeoscienceMap/BCGS\\_GM2001-10.pdf](http://cmscontent.nrs.gov.bc.ca/geoscience/PublicationCatalogue/GeoscienceMap/BCGS_GM2001-10.pdf)> [September 2020].
- Ferri, F., Dudka, S.F., Rees, C.J., Meldrum, D.G. and Willson, M.J. (2001b): Geology of the Uslika Lake area, north-central British Columbia (NTS 94C/2, 3 and 4); BC Ministry of Energy, Mines and Low Carbon Innovation, BC Geological Survey, Geoscience Map 2001-04, scale 1:50 000, URL <[http://cmscontent.nrs.gov.bc.ca/geoscience/PublicationCatalogue/GeoscienceMap/BCGS\\_GM2001-04.pdf](http://cmscontent.nrs.gov.bc.ca/geoscience/PublicationCatalogue/GeoscienceMap/BCGS_GM2001-04.pdf)> [September 2020].
- Ferry, J.M. and Watson, E.B. (2007): New thermodynamic models and revised calibrations for the Ti-in-zircon and Zr-in-rutile thermometers; *Contributions to Mineralogy and Petrology*, v. 154, p. 429–437, URL <<https://doi.org/10.1007/s00410-007-0201-0>>.
- Fisher, C.M., Paton, C., Pearson, D.G., Sarkar, C., Tersmette, D.B. and Chacko, T. (2017): Data reduction of laser ablation split-stream (LASS) analyses using newly developed features within Iolite – with applications to Lu-Hf + U-Pb in detrital zircon and Sm-Nd + U-Pb in igneous monazite; *Geochemistry, Geophysics, Geosystems*, v. 18, p. 4604–4622, URL <<https://doi.org/10.1002/2017GC007187>>.
- Fisher, C.M., Vervoort, J.D. and DuFrane, S.A. (2014): Accurate Hf isotope determinations of complex zircons using the ‘laser ablation split stream’ method; *Geochemistry, Geophysics, Geosystems*, v. 15, p. 121–139, URL <<https://doi.org/10.1002/2013GC004962>>.
- Garnett, J.A. (1972): Preliminary geological map of part of Hogem batholith, Duckling Creek area (parts of NTS 93N/13, 14; 94C/3, 4); BC Ministry of Energy, Mines and Low Carbon Innovation, BC Geological Survey, Preliminary Map 09, scale 1:63 360.
- Garnett, J.A. (1978): Geology and mineral occurrences of the southern Hogem batholith; BC Ministry of Energy, Mines and Low Carbon Innovation, BC Geological Survey, Bulletin 70, 75 p., URL <[http://cmscontent.nrs.gov.bc.ca/geoscience/PublicationCatalogue/Bulletin/BCGS\\_B070.pdf](http://cmscontent.nrs.gov.bc.ca/geoscience/PublicationCatalogue/Bulletin/BCGS_B070.pdf)> [September 2020].
- Giroux, G. and Lindinger, L.J. (2012): Summary report on the Lorraine-Jajay property, Omenica Mining Division, BC; Report 09-2012 prepared for Lorraine Copper Corp., 122 p., URL <[http://www.sedar.com/issuers/issuers\\_en.htm](http://www.sedar.com/issuers/issuers_en.htm)> [September 2020].
- Ickert, R. (2013): Algorithms for estimating uncertainties in initial radiogenic isotope ratios and model ages; *Chemical Geology*, v. 340, p. 131–138, URL <<https://doi.org/10.1016/j.chemgeo.2013.01.001>>.
- Lee, R.G., Byrne, K., D’Angelo, M., Hart, C.J.R., Hollings, P., Gleeson, S.A. and Alfaro, M. (2020): Using zircon trace element composition to assess porphyry copper potential of the Guichon Creek batholith and Highland Valley Copper deposit, south-central British Columbia; *Mineralium Deposita*, URL <<https://doi.org/10.1007/s00126-020-00961-1>>.
- Lee, R.G., Dilles, J.H., Tosdal, R.M., Wooden, J.L. and Mazdab, F.K. (2017): Magmatic evolution of granodiorite intrusions at the El Salvador porphyry copper deposit, Chile, based on trace element composition and U/Pb age of zircons; *Economic Geology*, v. 112, no. 2, p. 245–273, URL <<https://doi.org/10.2113/econgeo.112.2.245>>.
- Lord, C.S. (1948): McConnel Creek map-area, Cassiar District, British Columbia; Geological Survey of Canada, Memoir 251, 82 p., URL <<https://doi.org/10.4095/101588>>.
- Lord, C.S. (1949): McConnell Creek, Cassiar District, British Columbia; Geological Survey of Canada, Map 962A, scale 1 inch to 4 miles, URL <<https://doi.org/10.4095/106938>>.
- Lu, Y., Loucks, R.R., Fiorentini, M., McCuaig, T.C., Evans, N.J., Yang, Z., Hou, Z., Kirkland, C.L., Parra-Avila, L.A. and Kobussen, A. (2016): Zircon compositions as a pathfinder for porphyry Cu±Mo±Au deposits; Chapter 13 in *Tectonic and Metallogeny of the Tethyan Orogenic Belt*, J.P. Richards (ed.), Society of Economic Geologists, Special Volume 19, p. 329–348, URL <<https://doi.org/10.5382/SP.19.13>>.
- Milidragovic, D., Zagorevski, A., Weis, D., Joyce, N. and Chapman, J.B. (2018): Picrite ‘intelligence’ from the Middle-Late Triassic Stikine arc: composition of mantle wedge asthenosphere; *Lithos*, v. 308–309, p. 446–461, URL <<https://doi.org/10.1016/j.lithos.2018.03.014>>.
- Mortensen, J.K., Ghosh, D.K. and Ferri, F. (1995): U-Pb geochronology of intrusive rocks associated with copper-gold porphyry deposits in the Canadian Cordillera; Canadian Institute of Mining, Metallurgy and Petroleum, Special Volume 46, p. 142–158, URL <<https://store.cim.org/fr/u-pb-geochronology-of-intrusive-rocks-associated-with-copper-gold-porphyry-deposits-in-the-canadian-cordillera>> [October 2020].
- Nixon, G.T. and Peatfield, G.R. (2003): Geological setting of the Lorraine Cu-Au porphyry deposit, Duckling Creek Syenite Complex, north-central British Columbia; BC Ministry of Energy, Mines and Low Carbon Innovation, BC Geological Survey Open File 2003-4, 24 p., URL <[http://cmscontent.nrs.gov.bc.ca/geoscience/PublicationCatalogue/OpenFile/BCGS\\_OF\\_2003-04.pdf](http://cmscontent.nrs.gov.bc.ca/geoscience/PublicationCatalogue/OpenFile/BCGS_OF_2003-04.pdf)> [September 2020].
- Ootes, L., Bergen, A.L., Milidragovic, D., Graham, B. and Simmonds, R. (2019): Preliminary geology of northern Hogem batholith, Quesnel terrane, north-central British Columbia; in *Geological Fieldwork 2018*, BC Ministry of Energy, Mines and Low Carbon Innovation, BC Geological Survey, Paper 2019-01, p. 31–53, URL <[http://cmscontent.nrs.gov.bc.ca/geoscience/PublicationCatalogue/Paper/BCGS\\_P2019-01-03\\_Ootes.pdf](http://cmscontent.nrs.gov.bc.ca/geoscience/PublicationCatalogue/Paper/BCGS_P2019-01-03_Ootes.pdf)> [September 2020].
- Ootes, L., Bergen, A.L., Milidragovic, D. and Jones, G.O. (2020a): Bedrock geology of the northern Hogem batholith and its surroundings, north-central British Columbia; BC Ministry

- of Energy, Mines and Low Carbon Innovation, BC Geological Survey, Open File 2020-02, scale 1:50 000, URL <[http://cmscontent.nrs.gov.bc.ca/geoscience/Publication-Catalogue/OpenFile/BCGS\\_OF2020-02.pdf](http://cmscontent.nrs.gov.bc.ca/geoscience/Publication-Catalogue/OpenFile/BCGS_OF2020-02.pdf)> [September 2020].
- Ootes, L., Bergen, A.L., Milidragovic, D., Jones, G.O., Camacho, A. and Friedman, R. (2020b): An update on the geology of northern Hogem batholith and its surroundings, north-central British Columbia; *in* Geological Fieldwork 2019, BC Ministry of Energy, Mines and Low Carbon Innovation, BC Geological Survey Paper 2020-01, p. 25–47, URL <[http://cmscontent.nrs.gov.bc.ca/geoscience/Publication-Catalogue/Paper/BCGS\\_P2020-01-03\\_Ootes.pdf](http://cmscontent.nrs.gov.bc.ca/geoscience/Publication-Catalogue/Paper/BCGS_P2020-01-03_Ootes.pdf)> [September 2020].
- Richards, J.P. (2013): Giant ore deposits formed by optimal alignments and combinations of geological processes; *Nature Geoscience*, v. 6, p. 911–916, URL <<https://doi.org/10.1038/ngeo1920>>.
- Roots, E.F. (1954): Geology and mineral deposits of Aiken Lake map-area, British Columbia; Geological Survey of Canada, Memoir 274, 246 p., URL <<https://doi.org/10.4095/101499>>.
- Sagan, M., Heaman, L.M., Pearson, D.G., Luo, Y. and Stern, R. (2020): Removal of continental lithosphere beneath the Canary archipelago revealed from a U-Pb age and Hf/O isotope study of modern sand detrital zircons; *Lithos*, v. 362–363, 18 p., URL <<https://doi.org/10.1016/j.lithos.2020.105448>>.
- Schiarizza, P. and Tan, S.H. (2005): Geology of the Johanson Lake area, parts of NTS 94D/8 and 9; BC Ministry of Energy, Mines and Low Carbon Innovation, BC Geological Survey Open File 2005-4, scale 1:50 000, URL <[http://cmscontent.nrs.gov.bc.ca/geoscience/PublicationCatalogue/OpenFile/BCGS\\_OF2005-04.pdf](http://cmscontent.nrs.gov.bc.ca/geoscience/PublicationCatalogue/OpenFile/BCGS_OF2005-04.pdf)> [September 2020].
- Shen, P., Hattori, K., Pan, H., Jackson, S. and Seitmuratova, E. (2015): Oxidation condition and metal fertility of granitic magmas: zircon trace-element data from porphyry Cu deposits in the central Asian orogenic belt; *Economic Geology*, v. 110, no. 7, p. 1861–1878, URL <<https://doi.org/10.2113/econgeo.110.7.1861>>.
- Sillitoe, R.H. (2010): Porphyry copper systems; *Economic Geology*, v. 105, p. 3–41, URL <<http://dx.doi.org/10.2113/gsecongeo.105.1.3>>.
- Söderlund, U., Patchett, P.J., Vervoort, J.D. and Isachsen, C.E. (2004): The  $^{176}\text{Lu}$  decay constant determined by Lu-Hf and U-Pb isotope systematics of Precambrian mafic intrusions; *Earth and Planetary Science Letters*, v. 219, no. 3–4, p. 311–324, URL <[https://doi.org/10.1016/S0012-821X\(04\)00012-3](https://doi.org/10.1016/S0012-821X(04)00012-3)>.
- Sun, S. and McDonough, W.F. (1989): Chemical and isotopic systematics of oceanic basalts: implications for mantle composition and processes; *Geological Society of London, Special Publications*, v. 42, p. 313–345, URL <<https://doi.org/10.1144/GSL.SP.1989.042.01.19>>.
- Valley, J.W., Lackey, J.S., Casowie, A.J., Clechenko, C.C., Spicuzza, M.J., Basei, M.A.S., Bindeman, I.N., Ferreira, V.P., Sial, A.N., King, E.M., Peck, W.H., Sinha, A.K. and Wei, C.S. (2005): 4.4 billion years of crustal maturation: oxygen isotope ratios of magmatic zircon; *Contributions to Mineralogy and Petrology*, v. 150, p. 561–580, URL <<https://doi.org/10.1007/s00410-005-0025-8>>.
- Vezelet, A., Pearson, D.G., Thomassot, E., Stern, R.A., Sarkar, C., Luo, Y. and Fisher, C.M. (2018): Hydrothermally-altered mafic crust as source for early Earth TTG: Pb/Hf/O isotope and trace element evidence from TTG of the Eoarchean Saglek Block, N. Labrador (electronic supplementary material); *Earth and Planetary Science Letters*, v. 503, p. 95–107, URL <<https://doi.org/10.1016/j.epsl.2018.09.015>>.
- Watson, E.B., Wark, D.A. and Thomas, J.B. (2006): Crystallization thermometers for zircon and rutile; *Contributions to Mineralogy and Petrology*, v. 151, p. 413–433, URL <<https://doi.org/10.1007/s00410-006-0068-5>>.
- Wilke, M. and Behrens, H. (1999): The dependence of the partitioning of iron and europium between plagioclase and hydrous tonalitic melt on oxygen fugacity; *Contributions to Mineralogy and Petrology*, v. 137, p. 102–114, URL <<https://doi.org/10.1007/s004100050585>>.
- Woodsworth, G.J. (1976): Plutonic rocks of McConnell Creek (94 D west half) and Aiken Lake (94 C east half) map-areas, British Columbia; Geological Survey of Canada, Paper 76-1A, p. 69–73, URL <<https://doi.org/10.4095/104166>>.

